

# $\Lambda$ effect in rotating hydrodynamic convection

P. J. Käpylä<sup>1</sup>

Institute for Solar Physics (KIS), Georges-Köhler-Alle 401a, 79110 Freiburg im Breisgau, Germany, email: [pkapyla@leibniz-kis.de](mailto:pkapyla@leibniz-kis.de)

March 11, 2026

## ABSTRACT

*Context.* Rotating anisotropic convection generates differential rotation in stellar convection zones.

*Aims.* The main aim is to compute the non-diffusive contribution ( $\Lambda$  effect) to angular momentum transport, described by Reynolds stress, from rotating turbulent convection.

*Methods.* Rotating hydrodynamic convection is simulated in Cartesian geometry at different latitudes and rotation rates. Large-scale flows are suppressed such that the Reynolds stress is due to non-diffusive effects.

*Results.* The radial angular momentum flux is downward (outward) for slow (fast) rotation. This is in contrast in prevailing theories in mean-field hydrodynamics where the radial transport is always downward. The outward transport at rapid rotation is due to thermal Rossby waves that manifest as elongated large-scale convection cells near the equator. The horizontal angular momentum flux is always equatorward, with increasing concentration toward the equator as in earlier Cartesian studies. The magnitudes of the  $\Lambda$  effect coefficients are roughly an order of magnitude lower than in the case of anisotropically forced turbulence or in analytic theories.

*Conclusions.* The current results highlight the tension between numerical simulations, widely used mean-field models, and solar observations. The mean-fields models have been remarkably successful in reproducing solar differential rotation but underlying assumptions regarding turbulence in these models seem to be at odds with 3D simulations. The current simulation results for the vertical (radial) angular momentum transport are in accordance with spherical shell simulations, where thermal Rossby waves are responsible for the generation of equatorial acceleration or solar-like differential rotation. Thermal Rossby waves are absent in the turbulence models of current mean-field theories and they have not been unambiguously detected in the Sun.

**Key words.** turbulence – convection

## 1. Introduction

Observations of the Sun and other stars with convective envelopes show that differential rotation is ubiquitous (e.g. Rüdiger et al. 2013; Reinhold & Gizon 2015). The main driver of differential rotation has long thought to be non-vanishing Reynolds stress due to the interaction of rotation and convective turbulence (e.g. Rüdiger 1989)

$$Q_{ij} = \overline{u_i u_j}, \quad (1)$$

where  $u_i = U_i - \overline{U}_i$  is the fluctuating velocity and where the overbar denotes a suitably defined average. More specifically, the off-diagonal components of  $Q_{ij}$  have non-diffusive contributions in anisotropic turbulence that are proportional to the angular velocity  $\Omega$  which lead to generation of differential rotation. This is more commonly known as the  $\Lambda$  effect (e.g. Rüdiger 1980).

The  $\Lambda$  effect has been studied with simulations of anisotropically forced turbulence (Käpylä & Brandenburg 2008; Käpylä 2019b,a; Berekat et al. 2021). These results have confirmed the existence of the  $\Lambda$  effect and are in broad agreement with mean-field hydrodynamics (Rüdiger 1989). Convection simulations show qualitatively similar results at slow rotation (e.g. Pulkkinen et al. 1993; Rüdiger et al. 2005, 2019; Hupfer et al. 2005; Rüdiger & Küker 2021), but differences arise at rapid rotation where, for example, the radial angular momentum flux changes sign (Chan 2001; Käpylä et al. 2004). The latter arises due to large-scale wave-like convective modes also known as Busse columns, banana cells, or thermal Rossby waves that appear as tilted columns in an equatorial latitude belt (e.g. Busse 2002; Aurnou et al. 2007); see Käpylä (2023) and Mori & Hotta

(2023) for recent analyses of the associated angular momentum transport. Mean-field theories of stellar angular momentum transport (e.g. Kitchatinov & Rüdiger 1995; Kitchatinov & Rüdiger 2005; Kleorin & Rogachevskii 2006) do not include such large-scale convective modes and therefore the accuracy of their predictions in the case of convection is uncertain. The main goal of the current study is to compute the  $\Lambda$  effect from convection using a comprehensive set of simulations at varying rotation rates for the first time.

The paper is organized as follows: Section 2 introduces the  $\Lambda$  effect in the framework of mean-field hydrodynamics, Section 3 describes the model. In Section 4 the results of the study are discussed and in Section 5 the conclusions are presented.

## 2. Mean-field theory and the $\Lambda$ effect

The Reynolds stress in rotating turbulence can be written as

$$Q_{ij} = Q_{ij}^{(0)} + Q_{ij}^{(\Omega)} + Q_{ij}^{(S)}, \quad (2)$$

where  $Q_{ij}^{(0)}$  is present in the absence of rotation or shear,  $Q_{ij}^{(\Omega)}$  is due to rotation, and  $Q_{ij}^{(S)}$  is due to shear. Assuming the large-scale fields vary slowly in space and time, we write an ansatz

$$Q_{ij} = Q_{ij}^{(0)} + \Lambda_{ijk} \Omega_k - \mathcal{N}_{ijkl} \frac{\partial \overline{U}_k}{\partial x_l}, \quad (3)$$

where  $\Lambda_{ijk}$  and  $\mathcal{N}_{ijkl}$  are third and fourth rank tensors, respectively, and  $\Omega$  is the mean angular velocity. The appearance of cross-correlations requires two preferred directions (e.g. Rüdiger

1989). The gravity ( $\mathbf{g}$ ) and angular velocity ( $\mathbf{\Omega}$ ) vectors fulfill this requirement in rotating convection. However, in such cases large-scale flows are produced due to the  $\Lambda$  effect, and disambiguation of  $Q_{ij}^{(\Omega)}$  and  $Q_{ij}^{(S)}$  is impossible using a single simulation. To circumvent this complication the mean flows can be removed artificially (e.g. Rüdiger et al. 2019; Barekat et al. 2021). Thus  $Q_{ij}^{(S)}$  vanishes, and the Reynolds stress reads

$$Q_{ij} = Q_{ij}^{(0)} + Q_{ij}^{(\Omega)}, \quad (4)$$

where the rotation-generated stress is

$$Q_{ij}^{(\Omega)} = Q_{ij} - Q_{ij}^{(0)}. \quad (5)$$

The non-diffusive stress corresponding to the  $\Lambda$  effect is then

$$Q_{ij}^{(\Omega)} = \Lambda_{ijk} \Omega_k, \quad (6)$$

which can be extracted from a single experiment because off-diagonal components of  $Q_{ij}^{(0)}$  vanish. The horizontal, meridional, and vertical components of the  $\Lambda$  effect are given by

$$Q_{\theta\phi}^{(\Omega)} = \nu_{t0} \Omega H \cos \theta, \quad (7)$$

$$Q_{r\theta}^{(\Omega)} = \nu_{t0} \Omega M \sin \theta \cos \theta, \quad (8)$$

$$Q_{r\phi}^{(\Omega)} = \nu_{t0} \Omega V \sin \theta, \quad (9)$$

where  $\nu_{t0}$  is a reference value of turbulent viscosity. The factor  $\nu_{t0} \Omega$  is used for normalization, whereas  $V$ ,  $H$ , and  $M$  are dimensionless position-dependent functions.

It is important to bear in mind that Equations (7) to (9) are parametrizations that derive from symmetry properties but take no stand on the physical origin of the stress. Furthermore, Equations (7) to (9) are not limited to low Reynolds numbers which is the case for results derived under the first-order smoothing approximation (FOSA).

### 3. The model

The model is the same as in several earlier studies (e.g. Käpylä 2024, and references therein). The equations for compressible hydrodynamics

$$\frac{D \ln \rho}{Dt} = -\nabla \cdot \mathbf{u}, \quad (10)$$

$$\frac{D \mathbf{u}}{Dt} = \mathbf{g} - \frac{1}{\rho} (\nabla p - \nabla \cdot 2\nu \rho \mathbf{S}) - 2\mathbf{\Omega} \times \mathbf{u}, \quad (11)$$

$$T \frac{Ds}{Dt} = -\frac{1}{\rho} [\nabla \cdot (\mathbf{F}_{\text{rad}} + \mathbf{F}_{\text{SGS}}) + \mathcal{C}] + 2\nu \mathbf{S}^2, \quad (12)$$

were solved, where  $D/Dt = \partial/\partial t + \mathbf{u} \cdot \nabla$  is the advective derivative,  $\rho$  is the density,  $\mathbf{u}$  is the velocity,  $\mathbf{g} = -g \hat{\mathbf{e}}_z$  is the acceleration due to gravity with  $g > 0$ ,  $p$  is the pressure,  $\nu$  is the constant kinematic viscosity,  $\mathbf{S}$  is the traceless rate-of-strain tensor with  $S_{ij} = \frac{1}{2}(u_{i,j} + u_{j,i}) - \frac{1}{3} \delta_{ij} \nabla \cdot \mathbf{u}$  and  $\mathbf{\Omega} = \Omega_0 (-\sin \theta, 0, \cos \theta)^T$  is the rotation vector, where  $\theta$  is the angle between  $\mathbf{\Omega}$  and  $\mathbf{g}$ .  $T$  is the temperature,  $s$  is the specific entropy,  $\mathbf{F}_{\text{rad}}$  and  $\mathbf{F}_{\text{SGS}}$  are the radiative and turbulent subgrid scale (SGS) fluxes, respectively, and  $\mathcal{C}$  describes surface cooling. The gas is assumed optically thick and fully ionized such that radiation is modeled via diffusion approximation. The ideal gas equation of state  $p = (c_p - c_v) \rho T = \mathcal{R} \rho T$  applies, where  $\mathcal{R}$  is the gas constant, and  $c_p$  and  $c_v$  are the specific heats at constant pressure and volume, respectively. The radiative flux

is  $\mathbf{F}_{\text{rad}} = -K \nabla T$ , where  $K$  is the radiative heat conductivity given by  $K = 16 \sigma_{\text{SB}} T^3 / (3 \kappa \rho)$ , where  $\sigma_{\text{SB}}$  is the Stefan-Boltzmann constant and  $\kappa$  is the opacity. The Kramers opacity law  $\kappa = \kappa_0 (\rho/\rho_0)^a (T/T_0)^b$  with  $a = 1$  and  $b = -7/2$  was used (Weiss et al. 2004); see also Edwards (1990), Brandenburg et al. (2000), and (Dorch & Nordlund 2001) for early applications to convection simulations.

Turbulent SGS diffusivity is applied for the entropy fluctuations with  $\mathbf{F}_{\text{SGS}} = -\rho T \chi_{\text{SGS}} \nabla s'$ , where  $s'(\mathbf{x}) = s(\mathbf{x}) - \bar{s}(z)$  and where the overbar indicates horizontal averaging.  $\chi_{\text{SGS}}$  is constant throughout the domain and  $\bar{\mathbf{F}}_{\text{SGS}} \approx 0$  because the SGS diffusivity operates on the entropy fluctuations. The surface cooling is given by  $\mathcal{C} = f(z) c_p \rho (T - T_{\text{cool}}) / \tau_{\text{cool}}$ , where  $\tau_{\text{cool}} = 0.4 \sqrt{d/g}$  is a cooling timescale,  $T = e/c_v$  is the temperature where  $e$  is the internal energy, and where  $T_{\text{cool}} = T_{\text{top}}$  corresponds to the fixed value at the upper boundary.

#### 3.1. Geometry, initial and boundary conditions

The computational domain is a rectangular box where  $z_{\text{bot}} \leq z \leq z_{\text{top}}$  is the vertical coordinate, with  $z_{\text{bot}}/d = -0.45$ ,  $z_{\text{top}}/d = 1.05$ , and where  $d$  is the depth of the initially isentropic layer (see below). The horizontal coordinates  $x$  and  $y$  are given by  $-2d \leq (x, y) \leq 2d$ . The initial stratification consists of three layers. The two lower layers are polytropic with polytropic indices  $n_1 = 3.25$  ( $z_{\text{bot}}/d \leq z/d < 0$ ) and  $n_2 = 1.5$  ( $0 \leq z/d \leq 1$ ). The uppermost layer above  $z/d = 1$  is initially isothermal. The initial velocity follows a Gaussian-noise distribution with amplitude on the order of  $10^{-4} \sqrt{d/g}$ .

The horizontal boundaries are periodic. The vertical boundaries are impenetrable and stress-free for the flow such that  $u_{x,z} = u_{y,z} = u_z = 0$ . The temperature gradient at the bottom boundary is given by  $\partial_z T = -F_{\text{bot}}/K_{\text{bot}}$ , where  $F_{\text{bot}}$  is the fixed input flux and  $K_{\text{bot}}(x, y, z_{\text{bot}})$  is the heat conductivity at  $z = z_{\text{bot}}$ . Constant temperature  $T = T_{\text{top}}$  is assumed on the top boundary.

#### 3.2. Units, control parameters, and simulation strategy

The units of length, time, density, and entropy are given by  $[x] = d$ ,  $[t] = \sqrt{d/g}$ ,  $[\rho] = \rho_0$ ,  $[s] = c_p$ , where  $\rho_0$  is the initial value of density at  $z = z_{\text{top}}$ . The profile  $f(z) = 1$  above  $z/d = 1$  and  $f(z) = 0$  below  $z/d = 1$ , connecting smoothly over a width of  $0.025d$ , and  $\xi_0 = H_p^{\text{top}}/d = \mathcal{R} T_{\text{top}}/gd$  sets the initial pressure scale height at the surface. The Prandtl number based on the radiative heat conductivity is  $\text{Pr}(\mathbf{x}, t) = \nu/\chi(\mathbf{x}, t)$ , where  $\chi(\mathbf{x}, t) = K(\mathbf{x}, t)/c_p \rho(\mathbf{x}, t)$ . SGS Prandtl number is given by  $\text{Pr}_{\text{SGS}} = \nu/\chi$ .

Rayleigh number based on the energy flux is given by

$$\text{Ra}_{\text{F}} = \frac{g H^4 F_{\text{bot}}}{c_p \rho T \nu \chi^2}. \quad (13)$$

A diffusion-free Rayleigh number can be constructed using  $\text{Re}_{c_s} = c_s H/\nu$ , via

$$\text{Ra}_{\text{F}}^c = \frac{\text{Ra}_{\text{F}} \text{Pr}^2}{\text{Re}_{c_s}^3} = \frac{g H F_{\text{bot}}}{c_p \rho T c_s^3}. \quad (14)$$

Assuming  $H = H_T \equiv c_p T/g$ ,  $\text{Ra}_{\text{F}}^c$  reduces to the dimensionless normalized flux (e.g. Brandenburg et al. 2005):

$$\mathcal{F}_n = F_{\text{bot}}/\rho c_s^3. \quad (15)$$

In rotating simulations, a flux-based diffusion-free modified Rayleigh number is given by (e.g. Christensen 2002; Christensen & Aubert 2006; Käpylä 2024)

$$\text{Ra}_F^* = \frac{\text{Ra}_F}{\text{Pr}^2 \text{Ta}^{3/2}}, \quad (16)$$

where  $\text{Ta} = 4\Omega_0^2 d^4 / \nu^2$  is the Taylor number. This can be recast into a flux-based Coriolis number (Käpylä 2024; Bekki 2025)

$$\text{Co}_F = \frac{2\Omega_0 H}{u_*} = 2\Omega_0 H \left( \frac{\rho}{F_{\text{bot}}} \right)^{1/3} = (\text{Ra}_F^*)^{-1/3}, \quad (17)$$

with  $u_* \equiv (F_{\text{bot}}/\rho)^{1/3}$  and  $H = H_T$ .

In addition to explicit diffusion terms, the advective terms in Equations (10) to (12) are written in terms of a fifth-order up-winding derivative with a hyperdiffusive sixth-order correction with a flow-dependent diffusion coefficient; see Appendix B of Dobler et al. (2006). The PENCIL CODE<sup>1</sup> was used to produce the simulations (Pencil Code Collaboration et al. 2021).

### 3.3. Diagnostics quantities

The global Reynolds, SGS Péclet, and Coriolis numbers

$$\text{Re} = \frac{u_{\text{rms}}}{\nu k_1}, \quad \text{Pe}_{\text{SGS}} = \text{Pr}_{\text{SGS}} \text{Re}, \quad \text{Co} = \frac{2\Omega_0}{u_{\text{rms}} k_1}, \quad (18)$$

describe the importance of viscosity, SGS diffusion and rotation relative to advection, respectively. Here  $u_{\text{rms}}$  is the volume averaged rms-velocity and  $k_1 = 2\pi/d$  is an estimate of the largest eddies in the system. Typically  $\chi \ll \chi_{\text{SGS}}$  in the convection zone in the current simulations.

The overall anisotropy of the flow is characterized by the parameters

$$A_V = \frac{Q_{xx} + Q_{yy} - 2Q_{zz}}{Q}, \quad A_H = \frac{Q_{yy} - Q_{xx}}{Q}, \quad (19)$$

where  $Q = \text{Tr} Q_{ij}$ . The parameters  $A_V$  and  $A_H$  do not bear information about the scale dependence of anisotropy. This is revealed by spectral anisotropy parameters which are based on the power spectra of velocity components (e.g. Käpylä 2019a)

$$A_V(k) = \frac{E_x(k) + E_y(k) - 2E_z(k)}{E_K(k)}, \quad (20)$$

$$A_H(k) = \frac{E_y(k) - E_x(k)}{E_K(k)}, \quad (21)$$

where  $E_i \equiv u_i^2 = \int E_i(k) dk$ , and  $E_K(k) = \sum_i E_i(k)$ . Diagnostics are time-averaged over the statistically steady part of the simulations and horizontal or volume averages are additionally applied. Error estimates are given as the mean error of the mean where the number of turnover times is taken as the number of realizations.

## 4. Results

Some of the current slowly rotating runs use saturated snapshots of the progenitor Run K3h from Käpylä (2019c) as initial conditions whereas several sets of runs were run from scratch. In total, eight sets of runs with different  $\text{Co}_F$  with seven runs corresponding to different values of  $\theta$  were made; see Table 1.

**Table 1.** Summary of the runs.

Run	$\text{Ra}_F^*$	$\text{Ta}[10^6]$	$\theta$	$\text{Co}_F$	$\text{Co}$	$\text{Re}$	$\text{Ra}_t[10^6]$
A1	$2.5 \cdot 10^2$	0.01	$0^\circ$	0.28	0.07	38.9	4.1
A2	$2.5 \cdot 10^2$	0.01	$15^\circ$	0.28	0.07	38.9	4.1
A3	$2.5 \cdot 10^2$	0.01	$30^\circ$	0.28	0.07	38.9	4.2
A4	$2.5 \cdot 10^2$	0.01	$45^\circ$	0.28	0.07	39.0	4.1
A5	$2.5 \cdot 10^2$	0.01	$60^\circ$	0.28	0.06	39.0	4.2
A6	$2.5 \cdot 10^2$	0.01	$75^\circ$	0.28	0.07	38.9	4.2
A7	$2.5 \cdot 10^2$	0.01	$90^\circ$	0.28	0.07	38.9	4.0
B1	$3.1 \cdot 10^1$	0.04	$0^\circ$	0.55	0.13	39.4	4.3
B1	$3.1 \cdot 10^1$	0.04	$15^\circ$	0.55	0.13	39.4	4.3
B3	$3.1 \cdot 10^1$	0.04	$30^\circ$	0.56	0.13	39.5	4.3
B4	$3.1 \cdot 10^1$	0.04	$45^\circ$	0.56	0.13	39.7	4.3
B5	$3.1 \cdot 10^1$	0.04	$60^\circ$	0.56	0.13	39.8	4.2
B6	$3.1 \cdot 10^1$	0.04	$75^\circ$	0.57	0.13	39.7	4.2
B7	$3.1 \cdot 10^1$	0.04	$90^\circ$	0.57	0.13	39.8	4.2
C1	$3.9 \cdot 10^0$	0.16	$0^\circ$	1.04	0.26	39.6	4.5
C2	$3.9 \cdot 10^0$	0.16	$15^\circ$	1.05	0.25	39.8	4.5
C3	$3.9 \cdot 10^0$	0.16	$30^\circ$	1.06	0.25	40.0	4.4
C4	$3.9 \cdot 10^0$	0.16	$45^\circ$	1.06	0.25	40.3	4.5
C5	$3.9 \cdot 10^0$	0.16	$60^\circ$	1.07	0.25	40.4	4.4
C6	$3.9 \cdot 10^0$	0.16	$75^\circ$	1.10	0.25	40.5	4.4
C7	$3.9 \cdot 10^0$	0.16	$90^\circ$	1.11	0.25	40.6	4.4
D1	$2.5 \cdot 10^{-1}$	1.0	$0^\circ$	2.33	0.64	39.6	5.1
D2	$2.5 \cdot 10^{-1}$	1.0	$15^\circ$	2.35	0.63	39.9	5.1
D3	$2.5 \cdot 10^{-1}$	1.0	$30^\circ$	2.35	0.62	40.6	5.1
D4	$2.5 \cdot 10^{-1}$	1.0	$45^\circ$	2.35	0.62	41.0	5.2
D5	$2.5 \cdot 10^{-1}$	1.0	$60^\circ$	2.39	0.61	41.4	5.1
D6	$2.5 \cdot 10^{-1}$	1.0	$75^\circ$	2.49	0.60	42.0	5.0
D7	$2.5 \cdot 10^{-1}$	1.0	$90^\circ$	2.57	0.60	42.5	4.9
E1	$3.1 \cdot 10^{-2}$	4.0	$0^\circ$	4.56	1.27	39.8	6.0
E2	$3.1 \cdot 10^{-2}$	4.0	$15^\circ$	4.56	1.27	40.0	6.0
E3	$3.1 \cdot 10^{-2}$	4.0	$30^\circ$	4.53	1.25	40.5	6.1
E4	$3.1 \cdot 10^{-2}$	4.0	$45^\circ$	4.50	1.23	41.3	6.2
E5	$3.1 \cdot 10^{-2}$	4.0	$60^\circ$	4.55	1.19	42.5	6.3
E6	$3.1 \cdot 10^{-2}$	4.0	$75^\circ$	4.72	1.14	44.6	6.2
E7	$3.1 \cdot 10^{-2}$	4.0	$90^\circ$	4.89	1.11	45.8	6.1
F1	$3.9 \cdot 10^{-3}$	16	$0^\circ$	9.16	2.62	38.6	7.6
F2	$3.9 \cdot 10^{-3}$	16	$15^\circ$	9.16	2.61	38.9	7.6
F3	$3.9 \cdot 10^{-3}$	16	$30^\circ$	9.16	2.57	39.5	7.7
F4	$3.9 \cdot 10^{-3}$	16	$45^\circ$	9.22	2.51	40.4	7.8
F5	$3.9 \cdot 10^{-3}$	16	$60^\circ$	9.33	2.38	42.6	7.8
F6	$3.9 \cdot 10^{-3}$	16	$75^\circ$	9.78	2.23	45.5	7.6
F7	$3.9 \cdot 10^{-3}$	16	$90^\circ$	10.2	2.40	42.2	7.4
G1	$2.5 \cdot 10^{-4}$	100	$0^\circ$	24.6	7.37	34.4	10.8
G2	$2.5 \cdot 10^{-4}$	100	$15^\circ$	24.5	7.30	34.7	11.0
G3	$2.5 \cdot 10^{-4}$	100	$30^\circ$	24.5	7.14	35.5	11.7
G4	$2.5 \cdot 10^{-4}$	100	$45^\circ$	24.3	6.91	36.6	12.8
G5	$2.5 \cdot 10^{-4}$	100	$60^\circ$	24.6	6.45	39.3	13.3
G6	$2.5 \cdot 10^{-4}$	100	$75^\circ$	25.9	5.77	43.9	11.6
G7	$2.5 \cdot 10^{-4}$	100	$90^\circ$	24.6	5.17	49.0	9.4
H1	$3.0 \cdot 10^{-5}$	400	$0^\circ$	51.0	17.05	29.7	15.9
H2	$3.0 \cdot 10^{-5}$	400	$15^\circ$	51.0	16.90	30.0	16.7
H3	$3.0 \cdot 10^{-5}$	400	$30^\circ$	50.7	16.64	30.5	18.2
H4	$3.0 \cdot 10^{-5}$	400	$45^\circ$	50.4	16.22	31.2	19.8
H5	$3.0 \cdot 10^{-5}$	400	$60^\circ$	50.4	15.07	33.6	20.3
H6	$3.0 \cdot 10^{-5}$	400	$75^\circ$	49.2	13.30	38.1	17.7
H7	$3.0 \cdot 10^{-5}$	400	$90^\circ$	45.0	12.03	42.1	14.5

**Notes.** All of the runs have initially  $\text{Ra}_F = 5.1 \cdot 10^{12}$ , corresponding to  $\mathcal{F}_n = 4.6 \cdot 10^{-6}$ ,  $\text{Pr}_{\text{SGS}} = 1$  such that  $\text{Pe}_{\text{SGS}} = \text{Re}$ , and  $\xi_0 = 0.054$ . The grid resolution in all runs is  $288^3$ .

<sup>1</sup> <https://pencil-code.org/>

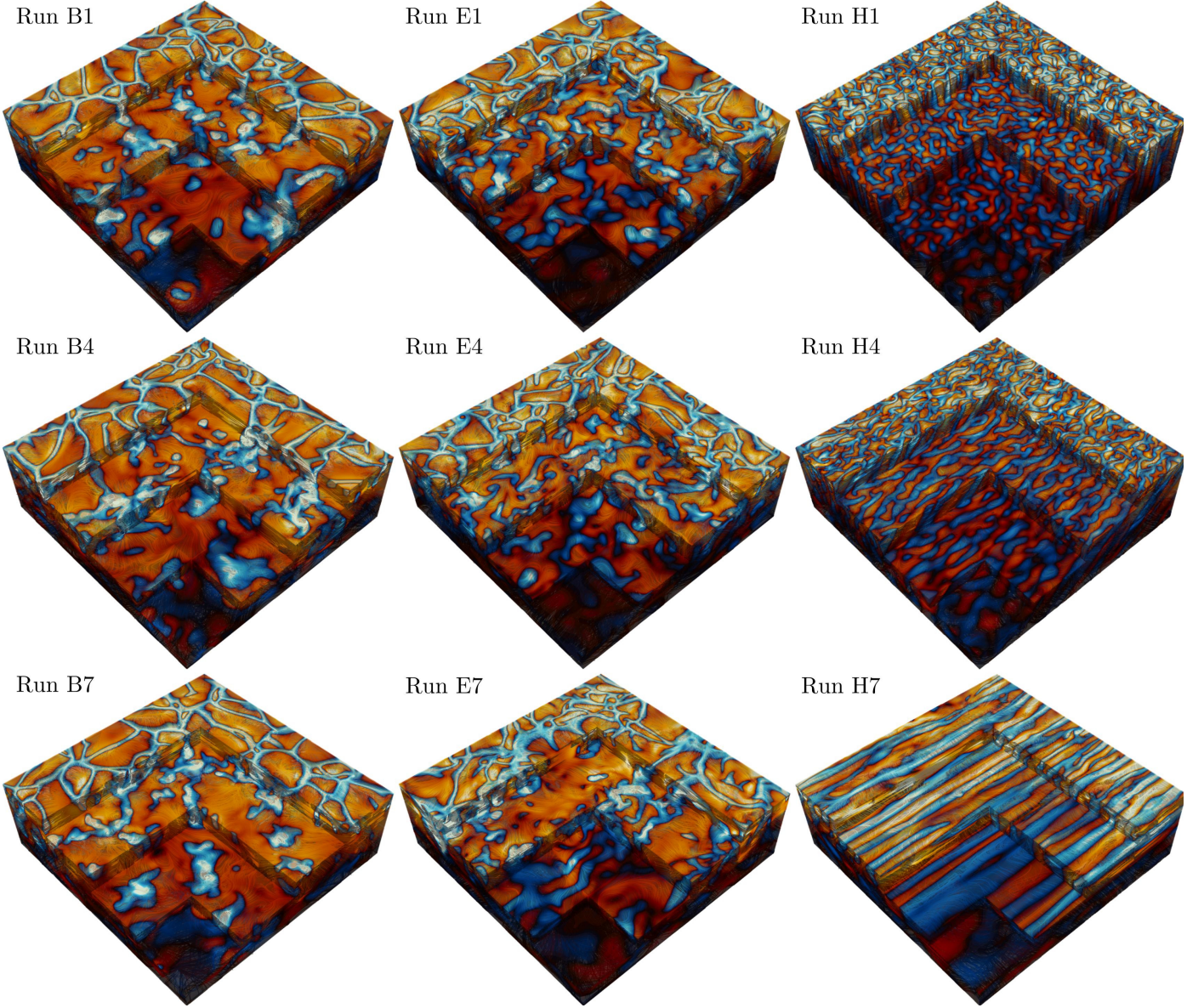


**Fig. 1.** Flow fields from Runs B1, B4, and B7 with  $Co_F \approx 0.55$  (left column), Runs E1, E4, and E7 with  $Co_F \approx 4.5 \dots 4.9$  (middle), and from Runs H1, H4, and H7 with  $Co_F \approx 12 \dots 17$  (right) at latitudes  $\theta = 0^\circ$  (top row),  $\theta = 45^\circ$  (middle), and  $\theta = 90^\circ$  (bottom).

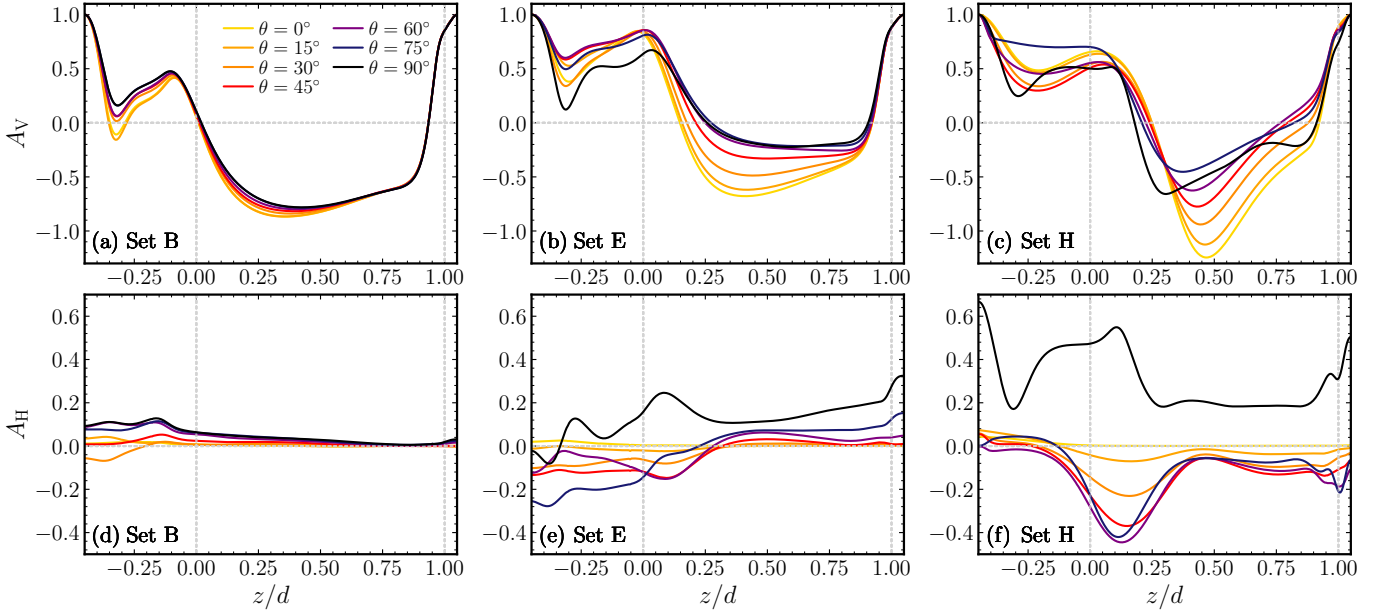
#### 4.1. Description of the flow fields

Figure 1 shows representative flow fields from runs with slow (Set B), intermediate (Set E), and rapid rotation (Set H) highlighting the transition from cellular convection at slow rotation to columnar convection at rapid rotation. The effects of rotation are not apparent in the most slowly rotating cases at any latitude; see the left column of Fig. 1. For intermediate rotation the average size of convection cells somewhat reduced and alignment of the convection cells with the rotation vector is discernible at the equator; see the middle column of Fig. 1. For rapid rotation the convection cells are significantly smaller and strongly aligned with the rotation vector; right column of Fig. 1. This is particularly apparent at the equator ( $\theta = 90^\circ$ , Run H7) where structures are aligned with the  $x$  direction. The dominant size of convective structures at the pole ( $\theta = 0^\circ$ ) was shown to follow the Coriolis-Inertial-Archimedean (CIA) scaling  $\ell \propto Co^{-1/2}$  in an earlier study (Käpylä 2024). A similar result was found for the equator ( $\theta = 90^\circ$ ), corresponding here to Runs B7, E7, and H7 shown

on the bottom row of Fig. 1, for spectra taken in the longitudinal ( $y$ ) direction in Bekki (2025). The evident horizontal anisotropy is a key ingredient leading to non-zero  $\Lambda$  effect.

#### 4.2. Anisotropy of turbulence

The vertical and horizontal  $\Lambda$  effects are to lowest order proportional to the turbulence anisotropies given by  $A_V$  and  $A_H$ , respectively (e.g. Rüdiger 1980). Representative results for  $A_V$  and  $A_H$  from runs with slow (Set B), intermediate (Set E), and rapid rotation (Set H) are shown in Fig. 2. In the slowly rotating cases  $A_V$  is negative throughout the convection zone; similarly to non-rotating cases (not shown). For  $Co_F \approx 0.55$  (Set B) the vertical anisotropy  $A_V$  remains practically constant in the upper part of the convection zone ( $z/d \gtrsim 0.65$ ) as a function of latitude. The absolute value of  $A_V$  decreases slightly in the lower part of the convection zone from the pole toward the equator. For intermediate (Set E) and rapid rotation (Set H) the latitudinal variation of  $A_V$  increases; see panels (b) and (c) of Fig. 2.



**Fig. 2.** Anisotropy parameters  $A_V$  (top row) and  $A_H$  (bottom) from runs in Set B with  $Co_F \approx 0.55$  (left), Set E with  $Co_F \approx 4.5 \dots 4.9$  (middle), and from Set H with  $Co_F \approx 12 \dots 17$  (right).

$A_V$  generally decreases from the pole to the equator. In the most rapidly rotating cases,  $A_V$  at the equator is again somewhat higher than at the low latitude cases; see panel (c) of Fig. 2. Furthermore, while  $A_V$  at the pole decreases for intermediate rotation, it is enhanced in the rapidly rotating cases.

The horizontal anisotropy  $A_H$  is much weaker than  $A_V$  for slow rotation because it is induced by rotation while the latter is an inherent property of convection.  $A_H$  vanishes at the pole due to symmetry and increases monotonically toward the equator for slow and intermediate rotation; see panels (d) and (e) of Fig. 2.  $A_H$  is negative for rapid rotation, Set H; see panel (f) of Fig. 2, which to lowest order would imply poleward angular momentum transport that promotes anti-solar differential rotation (e.g. Rüdiger 1980). However, the latter result is valid for slow rotation corresponding to  $Co \ll 1$ , which is not satisfied in the current rapidly rotating runs. Furthermore, this argument relies only on the magnitude of  $A_V$  while spatial scales of the horizontal flows are also very different in the latitudinal ( $x$ ) and longitudinal ( $y$ ) directions; see Figure 1.

To study the anisotropy in more detail, a spectral decomposition was made; see Equations (20) and (21). Representative results for  $A_V(k)$  and  $A_H(k)$  are shown in Figs. 3 and 4. Large scales are dominated by horizontal flows such that  $A_V(k) > 0$ , similarly as in the non-rotating case (not shown). The zero-crossing of  $A_V(k)$  occurs at a progressively higher normalized wavenumber  $\tilde{k} = k/k_1$  as the rotation rate increases. The negative  $A_V(k)$  at intermediate and large wavenumbers are responsible for  $A_V = \int A_V(k) dk < 0$  in the bulk of the convection zone in all cases. For slow rotation (Runs E[1,4,7])  $A_V(k)$  does not change appreciably as a function of  $\theta$ , whereas for the intermediate and rapid rotation runs the crossover from positive to negative  $A_V(k)$  occurs at a lower wavenumber; see the middle and right panels of Fig. 3.

As discussed above, the horizontal anisotropy becomes prominent only at rapid rotation, and it vanishes for  $\theta = 0^\circ$ ; see Fig. 4. For slow and intermediate rotation the main contribution to the overall positive  $A_H$  comes from large and intermediate scales; see the middle and right panels of Fig. 4. This can be un-

derstood as a consequence of rotational alignment of the largest convection cells that have the greatest Coriolis numbers. In the rapid rotation regime a similar trend is seen at large scales, but the behavior for  $k \gtrsim 10$  the latitudinal ( $x$ ) component dominates leading to  $A_H = \int A_H k dk < 0$ .

Turbulence becomes quasi-two-dimensional for sufficiently rapid rotation leading to diminishing velocity along  $\Omega$  (e.g. Müller & Thiele 2007). Strong density stratification has a similar effect along the direction of the gravitational acceleration (e.g. Boffetta 2023). The latter has been adopted as one of the building blocks for theories of angular momentum transport in stellar convection zones (e.g. Kitchatinov & Rüdiger 1993). This approach was generalized by Kitchatinov & Rüdiger (2005) who introduced an anisotropy parameter  $a$  that characterizes the difference between vertical and horizontal motions in the unperturbed case; see their equation A14. Assuming for simplicity that the scale ratio  $\ell_{\text{corr}}^2/L^2 = 1$ , the vertical anisotropy parameter  $A_V$  can be written in terms of  $a$  as follows:

$$A_V = \frac{1}{2} - \frac{1}{5}a, \quad (22)$$

such that  $a = \frac{5}{2}$  corresponds to isotropy. The range of  $A_V$  in Figure 3 inside the convection zone is roughly  $-0.2$  to  $-1.2$ , corresponding to  $a = 3.5 \dots 8.5$  which is significantly higher than the values typically used in mean-field approaches (e.g. Kitchatinov & Rüdiger 2005; Pipin & Kosovichev 2018).

### 4.3. Reynolds stress and $\Lambda$ effect

Horizontally and temporally averaged off-diagonal Reynolds stresses are shown in Figure 5. The stresses are assumed to be due to non-diffusive origin, and are attributed here to the  $\Lambda$  effect since horizontally averaged mean flows have been suppressed in the present simulations. The horizontal stress  $Q_{xy}$  is responsible for generating horizontal or latitude-dependent differential rotation in spherical coordinates.  $Q_{xy}$  is positive on average almost everywhere corresponding to equatorward flux of angular momentum; see the left column of Figure 5. For the slowest rotation rates the data is not sufficiently converged to rule out negative

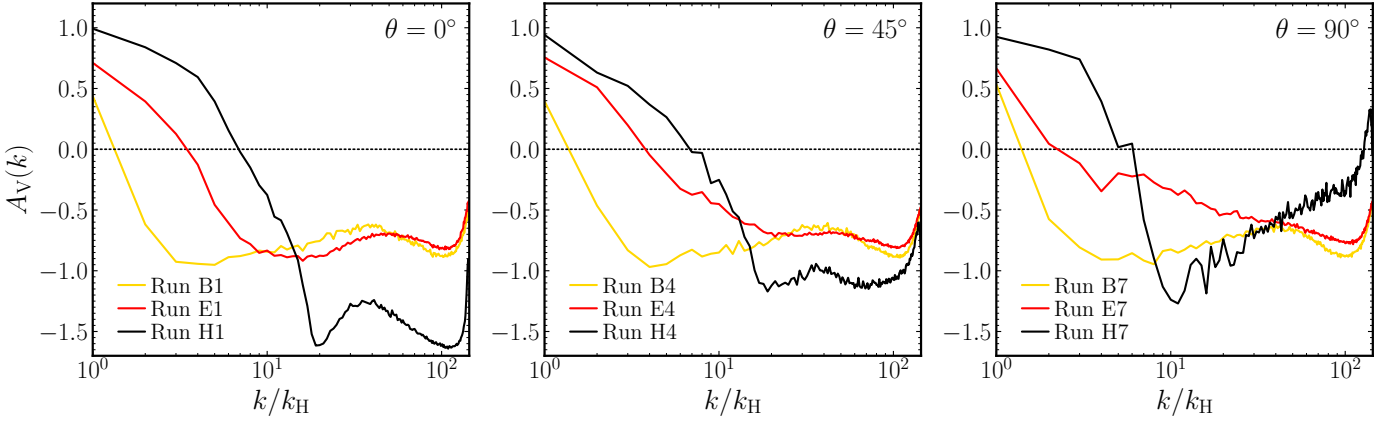


**Fig. 3.** Anisotropy parameter  $A_V(k)$  from runs with slow (Runs B1, B4, and B7), intermediate (Run E1, E4, and E7), and rapid rotation (Run H1, H4, and H7) at  $\theta = 0^\circ$  (left panel),  $\theta = 45^\circ$  (middle), and  $\theta = 90^\circ$  (right), respectively, near the middle of the convection zone at  $z/d = 0.49$ .

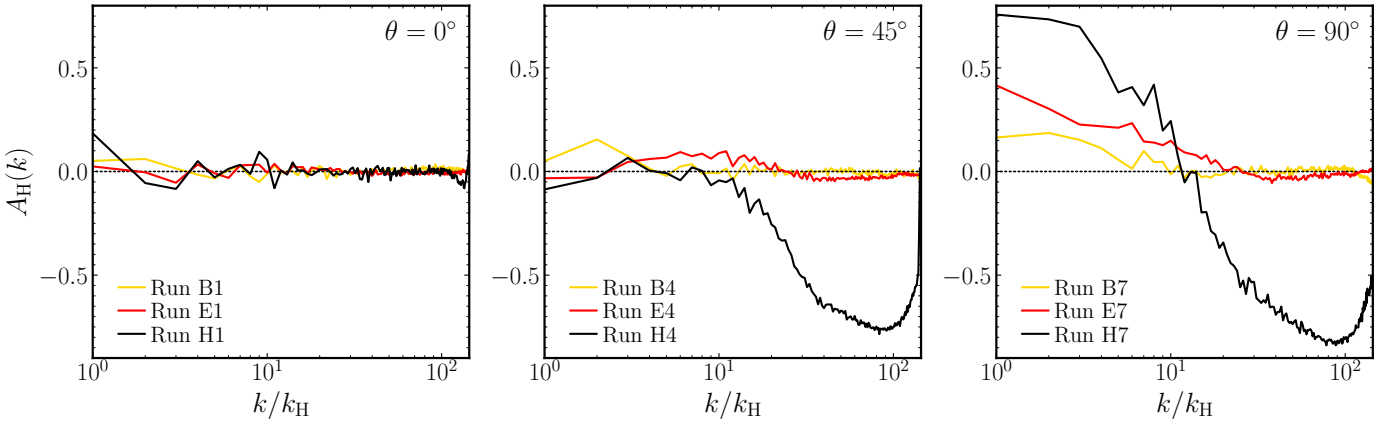


**Fig. 4.** Anisotropy parameter  $A_H(k)$  for the same runs as in Fig. 3.

values, which however are theoretically expected only in cases where shear is retained (Rüdiger et al. 2019). As the rotation rate is increased, the horizontal stress is increasingly concentrated near the equator; see the data for Sets E to H on the four bottom left panels of Figure 5. This behavior is commonly seen in f-plane simulations (e.g. Chan 2001; Käpylä et al. 2004; Hupfer et al. 2005) of convection but not in corresponding forced turbulence calculations (e.g. Käpylä & Brandenburg 2008; Käpylä 2019b). The main difference between the forced turbulence and convection setups is the lack of stratification and thermodynamics in the former such that, for example, thermal Rossby waves are not excited. Convective structures corresponding to the latter are the main contributor to  $Q_{xy}$  near the equator (see also Käpylä et al. 2011a). On the other hand, global convection simulations do not show a similar concentration of horizontal stress ( $Q_{\theta\phi}$ ) near the equator (e.g. Käpylä et al. 2011a). This is likely explained by the differences in geometry: in the current set-up the horizontal stress cannot generate a mean flow in the horizontally averaged sense because of the horizontal periodicity of the domain, whereas in global simulations the divergence of  $Q_{\theta\phi}$  leads to a mean flow. However, it is possible to generate mean flows that depend on  $x$  or  $y$  but vanish under a horizontal average even in the present geometry, although this has not been observed in the current simulations. A possible reason is that the horizontal size of the domain is too small or that the horizontal aspect ratio of the domain needs to be unequal to unity which ef-

fectively imposes a preferred direction (e.g. Guervilly & Hughes 2017; Currie et al. 2020). Furthermore, formation of large-scale vortices (e.g. Chan 2007; Käpylä et al. 2011b; Guervilly et al. 2014) is not observed in the current simulations most likely because the fluid Reynolds number is too low; see the discussion in Käpylä (2024).

The meridional stress  $Q_{xz}$  does not directly participate in the angular momentum transport but it has an indirect influence via the meridional flow. This component is predominantly negative for slow rotation ( $Co \lesssim 0.25$ , Sets A to C) with a magnitude similar to  $Q_{xy}$ . For  $Co \gtrsim 0.6$ ,  $Q_{xz}$  first changes sign for  $\theta = 75^\circ$  and at even more rapid rotation also for  $\theta = 60^\circ$ . This is in contrast to earlier forced turbulence simulations which yielded  $Q_{xz} < 0$  also for rapid rotation (e.g. Käpylä 2019b). It is possible that the difference is also due to the thermal Rossby waves that were absent in the isothermal forced turbulence models. The magnitude of  $Q_{xz}$  is less than the other off-diagonal components for  $Co \gtrsim 0.6$ . The impact of this stress component for stellar differential rotation has not been studied in detail.

The vertical stress  $Q_{yz}$  generates radial differential rotation. For slow rotation ( $Co \lesssim 0.6$ )  $Q_{yz}$  is negative almost everywhere and roughly proportional to  $\Omega$ . This agrees with analytic results and forced turbulence simulations (e.g. Käpylä & Brandenburg 2008; Käpylä 2019b). However, at sufficiently rapid rotation the sign of  $Q_{yz}$  changes near the equator where large positive values are observed; see the data for Sets F to H in the middle

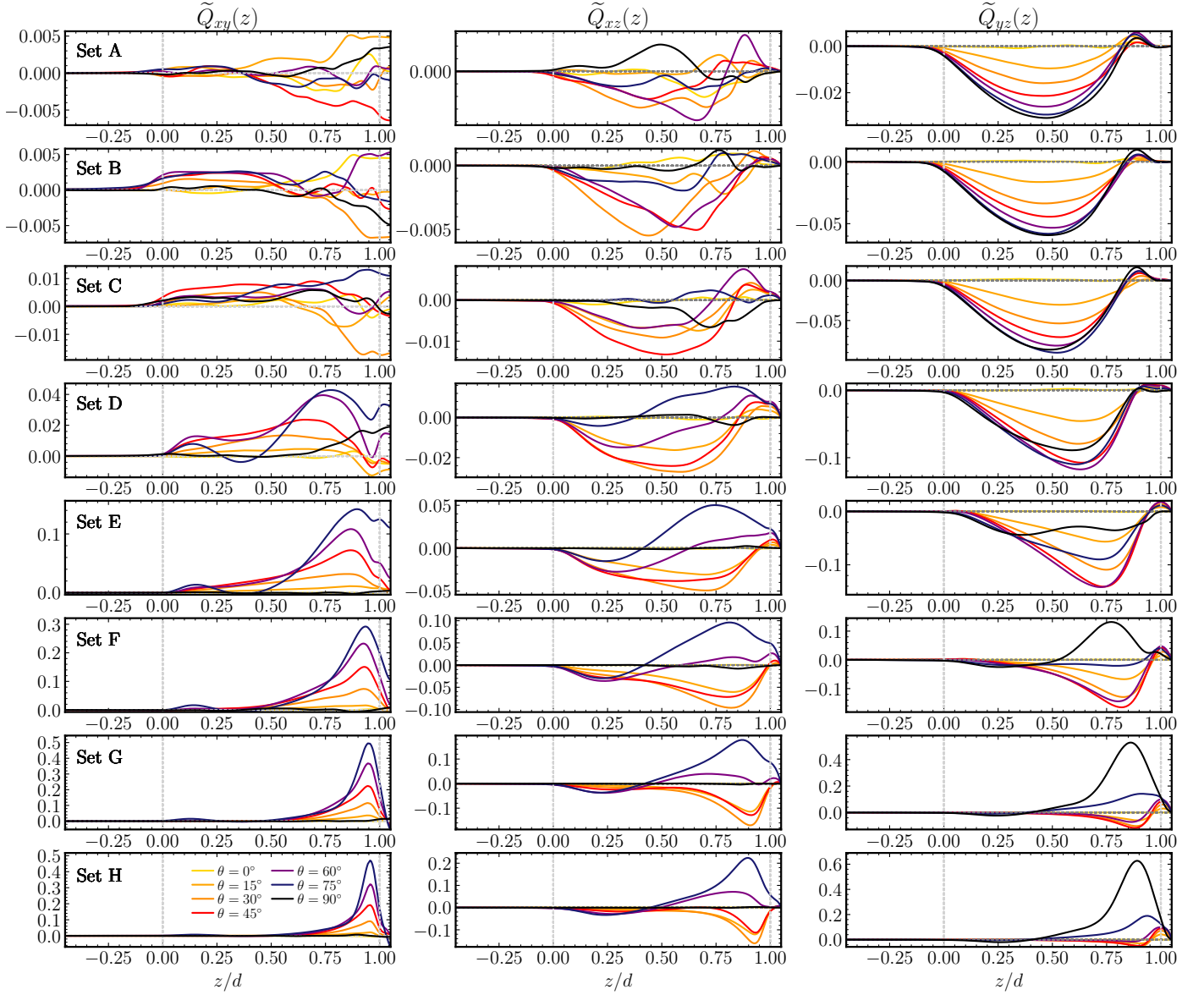


**Fig. 5.** Off-diagonal Reynolds stresses  $\tilde{Q}_{xy}$  (left column),  $\tilde{Q}_{xz}$  (middle), and  $\tilde{Q}_{yz}$  (right) from all of the runs. The set of runs and the corresponding  $\text{Co}_F$  are denoted on each row on the left panel.

column of Fig. 5. This feature is absent in isothermal forced turbulence models and is due to thermal Rossby waves that are excited in rotating convection (e.g. Busse 2002). Analyses of the radial stress  $Q_{r\phi}$ , corresponding to  $Q_{yz}$  in the current Cartesian geometry, in spherical shells and wedges have shown that the large-scale convective modes associated with the thermal Rossby waves produce the dominant contribution to  $Q_{r\phi}$  and produce equatorial acceleration (e.g. Käpylä 2023). This is in contrast to some hydrodynamic mean-field models where the radial stress vanishes for rapid rotation and equatorial acceleration is achieved via equatorward horizontal flux of angular momentum (e.g. Kitchatinov 2013).

The non-diffusive Reynolds stresses from Equations (7) to (9) can be represented in terms of the  $\Lambda$ -effect coefficients as

$$\mathcal{H} \equiv H \cos \theta = \frac{2}{15} \text{Co}^{-1} \tilde{Q}_{xy}, \quad (23)$$

$$\mathcal{M} \equiv M \sin \theta \cos \theta = \frac{2}{15} \text{Co}^{-1} \tilde{Q}_{xz}, \quad (24)$$

$$\mathcal{V} \equiv V \sin \theta = \frac{2}{15} \text{Co}^{-1} \tilde{Q}_{yz}, \quad (25)$$

where  $\nu_{t0} = \frac{4}{15} u_{\text{rms}} k_1$  was used, and where the tilde refers to normalization by  $u_{\text{rms}}^2$ . The functional form of  $\nu_{t0}$  is taken for a non-rotating case from the analytic study of (Kitchatinov et al. 1994). Results from numerical simulations of isotropically forced homogeneous turbulence tend to be somewhat higher; see Käpylä et al. (2020). Therefore the choice of  $\nu_{t0}$  in the normalization leads to some uncertainty in the absolute values of the coefficients. We follow the same procedure as in Käpylä (2019b), and expand the coefficients in powers of  $\sin^2 \theta$

$$H = \sum_1^{n_{\text{max}}} H^{(i)} \sin^{2n} \theta, \quad (26)$$

$$M = \sum_0^{n_{\text{max}}} M^{(i)} \sin^{2n} \theta, \quad (27)$$

$$V = \sum_0^{n_{\text{max}}} V^{(i)} \sin^{2n} \theta, \quad (28)$$

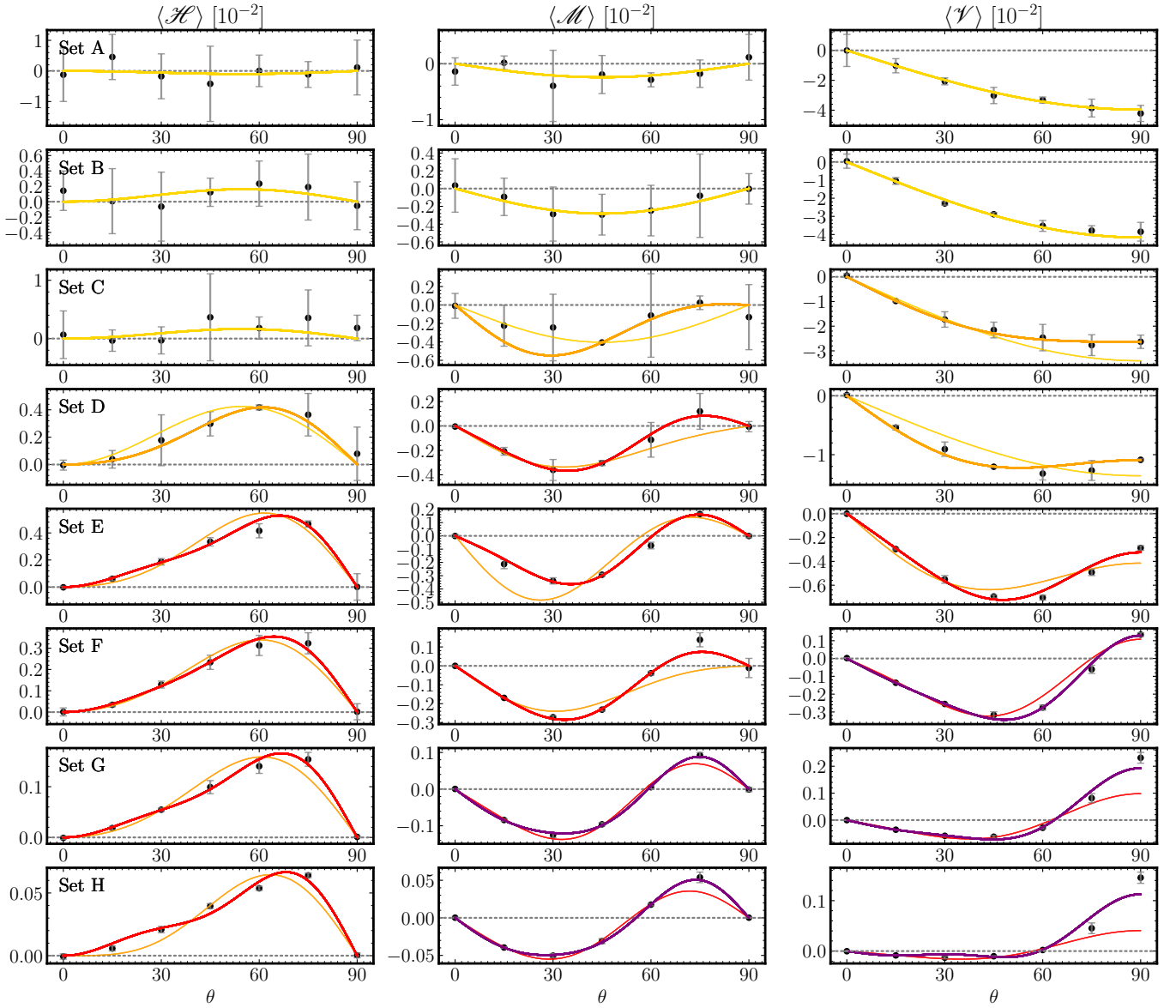


**Fig. 6.** Volume and time-averaged  $\Lambda$  coefficients  $\langle \mathcal{H} \rangle$  (left panels),  $\langle \mathcal{M} \rangle$  (middle), and  $\langle \mathcal{V} \rangle$  (right) from all sets of runs along with best fits to Eqs. (28) to (27). The thick lines show an adequate fit according to the criteria in the text and the thin lines show fits with one fewer coefficient for comparison. The colors denote the maximum number of coefficients  $n_{\max}$  taken into account in the fits such that  $n_{\max} = 0, 1, 2, 3$  correspond to yellow, orange, red, and purple, respectively.

where  $H^{(0)}$  is assumed to vanish due to symmetry. The Reynolds stresses vary as a function of height but here we apply volume averaging, denoted by angle brackets  $\langle \cdot \rangle$ , over the range  $0 \leq z/d \leq 1$  to simplify the analysis. The coefficients  $V$ ,  $H$ , and  $M$  were fitted with up to  $n_{\max} = 3$  using Equations (23) to (25) and Equations (26) to (28) with volume averaged numerical data for the Reynolds stresses. The fit was deemed accurate enough when the mean error of the mean between the numerical data and the reconstruction with the fitted coefficients did not decrease by more than ten per cent when an additional coefficient was taken into account. However,  $n_{\max}$  higher than 3 would be needed to fit the vertical stress  $\langle \bar{Q}_{yz} \rangle$  for the most rapidly rotating cases (Sets G and H) but this was not pursued. The numerical data as well as the fits are shown in Fig. 6 for all runs. Furthermore, Table 2 summarizes the fitted coefficients.

The horizontal  $\Lambda$  effect is positive for all rotation rates, although in the slowest rotation cases studied (Sets A, B, and C)

the results are not statistically significant. These results are in accordance with quasi-linear theory (e.g. Rüdiger 1989), where negative values  $\mathcal{H}$  are expected only when large-scale flows (Rüdiger et al. 2019) or magnetic fields (e.g. Kitchatinov & Rüdiger 2004; Käpylä 2019b) are present, both of which are absent in the current simulations. The concentration of the horizontal stress near the equator is reflected in the horizontal  $\Lambda$  effect coefficient  $\mathcal{H}$ , although this behavior is subdued in Fig. 6 due to the volume averaging. Nevertheless,  $\langle \mathcal{H} \rangle$  tends to have its maximum at the nearest latitude away from the equator for  $\text{Co} > 0.6$  (Sets E to H). This is reflected by the need to use coefficients up to  $H^{(3)}$  to fit the data already in Set E; see the second to fourth columns of Table 2. More data points at lower latitudes would be needed to determine the full latitude profile but this is out of the scope of the present study. In Käpylä (2019b) all of the  $H^{(i)}$  coefficients were found to be positive which is not the case for  $H^{(1)}$  in the present study.

**Table 2.** Summary of the fitted  $\Lambda$  coefficients.

Set	$H^{(1)}$	$H^{(2)}$	$H^{(3)}$	$M^{(0)}$	$M^{(1)}$	$M^{(2)}$	$M^{(3)}$	$V^{(0)}$	$V^{(1)}$	$V^{(2)}$	$V^{(3)}$
A	-0.26	–	–	-0.48	–	–	–	-3.96	–	–	–
B	0.42	–	–	-0.56	–	–	–	-4.17	–	–	–
C	0.43	–	–	-1.72	1.81	–	–	-3.85	1.22	–	–
D	0.39	0.96	–	-0.80	-0.57	1.91	–	-2.31	1.22	–	–
E	1.16	-2.02	2.99	-0.62	-1.47	3.02	–	-1.10	-0.45	1.22	–
F	0.62	-0.52	1.24	-0.66	-0.28	1.40	–	-0.55	0.39	-1.30	1.59
G	0.35	-0.67	0.99	-0.38	0.68	-1.48	1.71	-0.16	0.37	-1.01	0.99
H	0.18	-0.44	0.56	-0.18	0.42	-0.79	0.84	-0.05	0.34	-0.89	0.72

**Notes.** Values of all coefficients are boosted by a factor of  $10^2$ . A missing value indicates that the fit with fewer coefficients was deemed sufficiently accurate.

The volume-averaged meridional  $\Lambda$  effect  $\langle \mathcal{M} \rangle$ , shown in the middle column of Fig. 6, is negative for slow rotation up to around  $\text{Co} = 0.25$  (Set C). For more rapid rotation,  $\langle \mathcal{M} \rangle$  changes sign near the equator which was not observed in the forced turbulence simulations of Käpylä (2019b), but was present in earlier simulations by Käpylä & Brandenburg (2008). Pulkkinen et al. (1993)<sup>2</sup> reported  $M^{(0)} = -0.03$  and  $M^{(1)} = 0.06$ , although the quality of their fit is rather modest; see their Fig. 11. The signs coincide with the current Set C although the values are greater than in the current runs. This is possibly because mean flows were retained in the runs of Pulkkinen et al. (1993) that also contribute to the Reynolds stress; see (e.g. Rüdiger et al. 2019). For more rapid rotation (Sets D onward), at least three coefficients are needed to fit the data. The sign of  $M^{(0)}$  coincides with that in forced turbulence simulations of Käpylä (2019b) but the behavior of the higher order coefficients is more complex.

The vertical  $\Lambda$  effect  $\langle \mathcal{V} \rangle$  is negative for  $\text{Co}_F \lesssim 4.56$  (Sets A to E). In the two slowest rotating sets A and B, only the fundamental mode of the  $\Lambda$  effect, described by  $V^{(0)}$  is needed to fit the numerical data; see Table 2. The absolute value of  $V^{(0)}$  is of the order of 0.05 in the slowest rotation cases. The sign and functional form agree with forced turbulence simulations (e.g. Käpylä 2019b; Barekat et al. 2021) but the absolute value is an order of magnitude smaller in the current results although the vertical anisotropy of the flow as measured by  $\Lambda_V$  is similar in both cases; compare Fig. 2 with Fig. 3 of Barekat et al. (2021). For  $\text{Co} \gtrsim 2.5$  (Sets F to H), the sign of  $\langle \mathcal{V} \rangle$  changes near the equator. In the current results  $V^{(0)} < 0$  and  $V^{(3)} > 0$  everywhere, whereas  $V^{(1)} > 0$  and  $V^{(2)} < 0$  apart from Set E; see the three last columns in Table 2. In Käpylä (2019b),  $V^{(0)}$  is also predominantly negative, whereas  $V^{(1)} < 0$  and  $V^{(2)} > 0$  in contrast to the current results. Analytic studies do not typically consider coefficients higher than  $V^{(1)}$ ; see, for example, Kitchatinov & Rüdiger (2005); Pipin & Kosovichev (2018).

The qualitative differences between the analytic theories and isothermal forced turbulence simulations in comparison to the current results for the vertical  $\Lambda$  effect are likely due to the dominating influence of thermal Rossby waves that appear as tilted columnar convection cells near the equator (e.g. Käpylä 2023). Thermal Rossby waves are typically not captured by analytics that rely on simplified turbulence models and therefore a positive  $\langle \mathcal{V} \rangle$  for rapid rotation is absent in such theories. This applies also to analytic theories where the convective heat flux is taken into account (e.g. Kleorin & Rogachevskii 2006). However, Pipin & Kosovichev (2018) found that the standard mean-field theory

does yields a sign change of the vertical  $\Lambda$  effect for rapid rotation although the physical interpretation of this effect is currently unclear.

## 5. Conclusions

The current simulations show that the radial non-diffusive angular momentum transport, parameterized by the vertical  $\Lambda$  effect, is negative for slow rotation ( $\text{Co} \lesssim 1.3$ ) in rotating density-stratified convection. The horizontal  $\Lambda$  effect is positive, corresponding to equatorward angular momentum flux, for all rotation rates. These findings are in qualitative agreement with isothermal forced turbulence simulations (e.g. Käpylä & Brandenburg 2008; Käpylä 2019b; Barekat et al. 2021) and analytic mean-field theories (e.g. Kitchatinov & Rüdiger 1995; Kleorin & Rogachevskii 2006). For more rapid rotation the radial  $\Lambda$  effect changes sign and the horizontal flux is increasingly concentrated at low latitudes. The change of sign of the vertical  $\Lambda$  effect is due to the emergence of prograde propagating thermal Rossby waves which are not accounted for in analytic theories of angular momentum transport (e.g. Rüdiger 1989; Kitchatinov & Rüdiger 2005). In global convection simulations the thermal Rossby waves are the cause of solar-like differential rotation. On the other hand, thermal Rossby waves have not been observed in the Sun (e.g. Birch et al. 2024, and references therein), and if they are present, they must be much weaker than in simulations. Therefore the origin of solar and stellar differential rotation is related to the ongoing debate regarding the nature of convection in the Sun (e.g. Schumacher & Sreenivasan 2020; Hotta et al. 2023, and references therein), often referred to as convective conundrum (e.g. O’Mara et al. 2016).

The current study probes the hydrodynamic regime with simulations where the density stratification is much weaker than in stars and where the transition to optically thin photosphere is modeled rather crudely. Magnetic fields have been shown to strongly affect the angular momentum transport and large-scale flows in global simulations (e.g. Hotta et al. 2022; Hotta 2025; Käpylä 2023; Soderlund et al. 2025). Magnetic fields have also been shown to significantly influence the  $\Lambda$  effect in theoretical and idealized numerical studies (e.g. Kitchatinov & Rüdiger 2004; Käpylä 2019b,a). The inability to incorporate a realistic stratification or proper radiative surface possibly inhibit non-local entropy rain (e.g. Spruit 1997; Brandenburg 2016; Käpylä 2025) in the current studies. The effects to convective angular momentum transport of these aspects need to be addressed in future studies.

*Acknowledgements.* The simulations were performed using the resources granted by the Gauss Center for Supercomputing for the Large-Scale computing

<sup>2</sup> Their  $M^{(i)}$  corresponds to  $M^{(i-1)}$  of the current study.

project “Cracking the Convective Conundrum” in the Leibniz Supercomputing Centre’s SuperMUC-NG supercomputer in Garching, Germany. This work was supported in part by the Deutsche Forschungsgemeinschaft Heisenberg programme (grant No. KA 4825/4-1).

Soderlund, K. M., Wulff, P., Käpylä, P. J., & Aurnou, J. M. 2025, *MNRAS*, 541, 1816  
 Spruit, H. 1997, *Mem. Soc. Astron. Italiana*, 68, 397  
 Weiss, A., Hillebrandt, W., Thomas, H.-C., & Ritter, H. 2004, *Cox and Giuli’s Principles of Stellar Structure* (Cambridge, UK: Cambridge Scientific Publishers Ltd)

## References

Aurnou, J., Heimpel, M., & Wicht, J. 2007, *Icarus*, 190, 110  
 Barekat, A., Käpylä, M. J., Käpylä, P. J., Gilson, E. P., & Ji, H. 2021, *A&A*, 655, A79  
 Bekki, Y. 2025, *A&A*, 703, A262  
 Birch, A. C., Proxauf, B., Duvall, T. L., et al. 2024, *Physics of Fluids*, 36, 117136  
 Boffetta, G. 2023, *Atmosphere*, 14, 1688  
 Brandenburg, A. 2016, *ApJ*, 832, 6  
 Brandenburg, A., Chan, K. L., Nordlund, Å., & Stein, R. F. 2005, *AN*, 326, 681  
 Brandenburg, A., Nordlund, A., & Stein, R. F. 2000, in *Geophysical and Astrophysical Convection*, ed. P. A. Fox & R. M. Kerr, 85–105  
 Busse, F. H. 2002, *Phys. Fluids*, 14, 1301  
 Chan, K. L. 2001, *ApJ*, 548, 1102  
 Chan, K. L. 2007, *Astron. Nachr.*, 328, 1059  
 Christensen, U. R. 2002, *Journal of Fluid Mechanics*, 470, 115  
 Christensen, U. R. & Aubert, J. 2006, *Geophys. J. Int.*, 166, 97  
 Currie, L. K., Barker, A. J., Lithwick, Y., & Browning, M. K. 2020, *MNRAS*, 493, 5233  
 Dobler, W., Stix, M., & Brandenburg, A. 2006, *ApJ*, 638, 336  
 Dorch, S. B. F. & Nordlund, Å. 2001, *A&A*, 365, 562  
 Edwards, J. M. 1990, *MNRAS*, 242, 224  
 Guervilly, C. & Hughes, D. W. 2017, *Physical Review Fluids*, 2, 113503  
 Guervilly, C., Hughes, D. W., & Jones, C. A. 2014, *J. Fluid Mech.*, 758, 407  
 Hotta, H. 2025, *ApJ*, 985, 163  
 Hotta, H., Bekki, Y., Gizon, L., Noraz, Q., & Rast, M. 2023, *Space Sci. Rev.*, 219, 77  
 Hotta, H., Kusano, K., & Shimada, R. 2022, *ApJ*, 933, 199  
 Hupfer, C., Käpylä, P., & Stix, M. 2005, *Astron. Nachr.*, 326, 223  
 Käpylä, P. J. 2019a, *Astronomische Nachrichten*, 340, 744  
 Käpylä, P. J. 2019b, *A&A*, 622, A195  
 Käpylä, P. J. 2019c, *A&A*, 631, A122  
 Käpylä, P. J. 2023, *A&A*, 669, A98  
 Käpylä, P. J. 2024, *A&A*, 683, A221  
 Käpylä, P. J. 2025, *A&A*, 698, L13  
 Käpylä, P. J. & Brandenburg, A. 2008, *A&A*, 488, 9  
 Käpylä, P. J., Korpi, M. J., & Tuominen, I. 2004, *A&A*, 422, 793  
 Käpylä, P. J., Mantere, M. J., Guerrero, G., Brandenburg, A., & Chatterjee, P. 2011a, *A&A*, 531, A162  
 Käpylä, P. J., Mantere, M. J., & Hackman, T. 2011b, *ApJ*, 742, 34  
 Käpylä, P. J., Rheinhardt, M., Brandenburg, A., & Käpylä, M. J. 2020, *A&A*, 636, A93  
 Kitchatinov, L. L. 2013, in *Solar and Astrophysical Dynamos and Magnetic Activity*, ed. A. G. Kosovichev, E. de Gouveia Dal Pino, & Y. Yan, Vol. 294, 399–410  
 Kitchatinov, L. L., Pipin, V. V., & Rüdiger, G. 1994, *Astron. Nachr.*, 315, 157  
 Kitchatinov, L. L. & Rüdiger, G. 1993, *A&A*, 276, 96  
 Kitchatinov, L. L. & Rüdiger, G. 1995, *A&A*, 299, 446  
 Kitchatinov, L. L. & Rüdiger, G. 2004, *Astron. Nachr.*, 325, 496  
 Kitchatinov, L. L. & Rüdiger, G. 2005, *Astron. Nachr.*, 326, 379  
 Kleorin, N. & Rogachevskii, I. 2006, *Phys. Rev. E*, 73, 046303  
 Mori, K. & Hotta, H. 2023, *MNRAS*, 519, 3091  
 Müller, W.-C. & Thiele, M. 2007, *EPL (Europhysics Letters)*, 77, 34003  
 O’Mara, B., Miesch, M. S., Featherstone, N. A., & Augustson, K. C. 2016, *Adv. Space Res.*, 58, 1475  
 Pencil Code Collaboration, Brandenburg, A., Johansen, A., et al. 2021, *The Journal of Open Source Software*, 6, 2807  
 Pipin, V. V. & Kosovichev, A. G. 2018, *ApJ*, 854, 67  
 Pulkkinen, P., Tuominen, I., Brandenburg, A., Nordlund, A., & Stein, R. F. 1993, *A&A*, 267, 265  
 Reinhold, T. & Gizon, L. 2015, *A&A*, 583, A65  
 Rüdiger, G. 1980, *Geophys. Astrophys. Fluid Dynam.*, 16, 239  
 Rüdiger, G. 1989, *Differential Rotation and Stellar Convection. Sun and Solar-type Stars* (Berlin: Akademie Verlag)  
 Rüdiger, G., Egorov, P., & Ziegler, U. 2005, *Astron. Nachr.*, 326, 315  
 Rüdiger, G., Kitchatinov, L. L., & Hollerbach, R. 2013, *Magnetic Processes in Astrophysics: theory, simulations, experiments* (Wiley-VCH)  
 Rüdiger, G. & Küker, M. 2021, *A&A*, 649, A173  
 Rüdiger, G., Küker, M., Käpylä, P. J., & Strassmeier, K. G. 2019, *A&A*, 630, A109  
 Schumacher, J. & Sreenivasan, K. R. 2020, *Reviews of Modern Physics*, 92, 041001